© 2026 The Authors

Residual forearc peridotites recording the early magmatic stage of subduction initiation

I. Nishio, N. Akizawa, T. Ishii, K. Itano, A. Tamura, T. Morishita

Supplementary Information

The Supplementary Information includes:

- Samples and Analytical Methods
- Reconstructing Primary REE Contents in Clinopyroxene
- Influx-Free Open System Melting Models
- Best Fit Model Estimation
- Slab Derived Fluid Influx Open System Melting Models
- Compiled Forearc Spinel Data and Reference Data for Plots
- Tables S-1 to S-15
- Figures S-1 to S-12
- Supplementary Information References

Samples and Analytical Methods

The samples are four harzburgites (ODP125-778A-003R-CC-4-7, ODP125-779A-26R-02-47-50, ODP125-780C-10R-01-11-13, ODP125-780D-005X-01-0-4) from Conical seamount in the IBM forearc (Fig. S-1), which were collected during ODP Leg 125 Site 778A, 779A, 780C, and 780D (Fig. S-2) (Ishii *et al.*, 1992; Parkinson *et al.*, 1992; Parkinson and Pearce, 1998) and a lherzolite sample (BMRG08-111-3-6) from the northern part of the Tonga forearc, which was collected during the 1996 Boomerang Leg 8 cruise (Bloomer *et al.*, 1996; Wright *et al.*, 2000; Birner *et al.*, 2016, 2017). We use samples previously studied by Ishii *et al.* (1992) (IBM) and Birner *et al.* (2017) (Tonga). IBM harzburgite ODP125-778A-003R-CC-4-7 and Tonga lherzolite BMRG08-111-3-6 contain minor amounts of clinopyroxene (IBM: ~2 vol.%; Tonga: 9 vol.%). Plagioclase and garnet are absent in the samples, and the IBM samples are serpentinised.

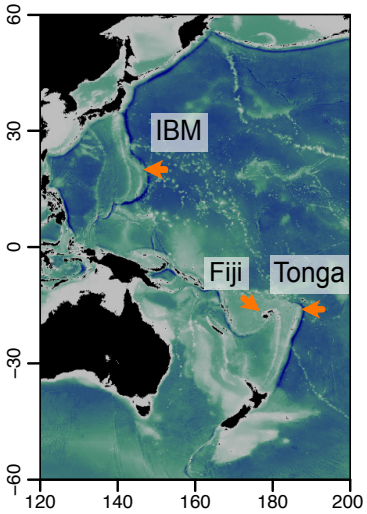

Figure S-1 A map of the western Pacific. Arrows in the IBM and Tonga represent the sample locations.

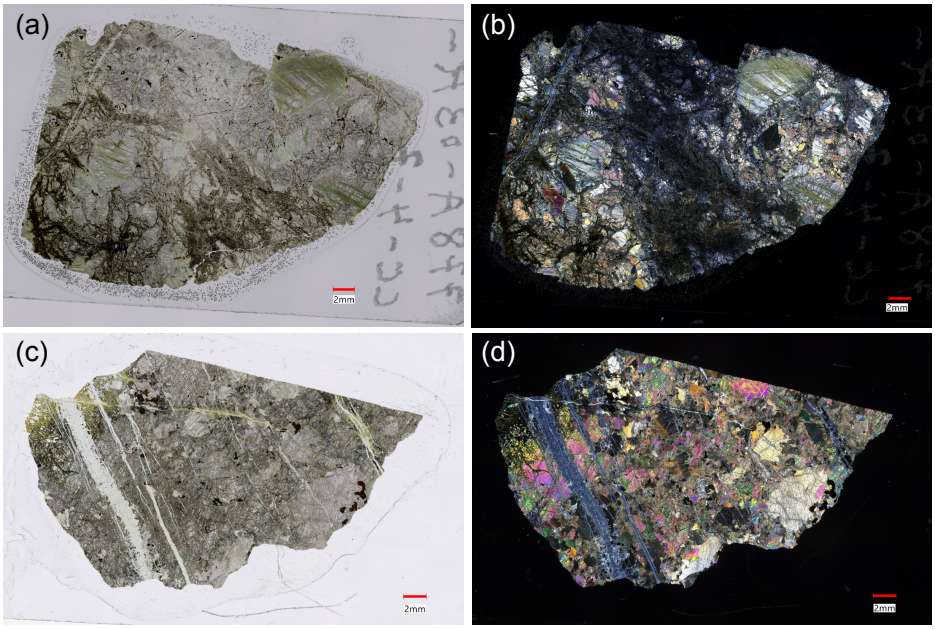

Figure S-2 Photomicrographs of IBM harzburgite and Tonga lherzolite samples. **(a and b)** The harzburgite sample (ODP125-778A-003R-CC-4–7) from the Conical Seamount IBM forearc region. **(c and d)** The lherzolite sample (BMRG08-111-3-6) from the Northern Tonga forearc region. The red colour bar indicates 2 millimetres. (b) and (d) were taken under cross-polarized light.

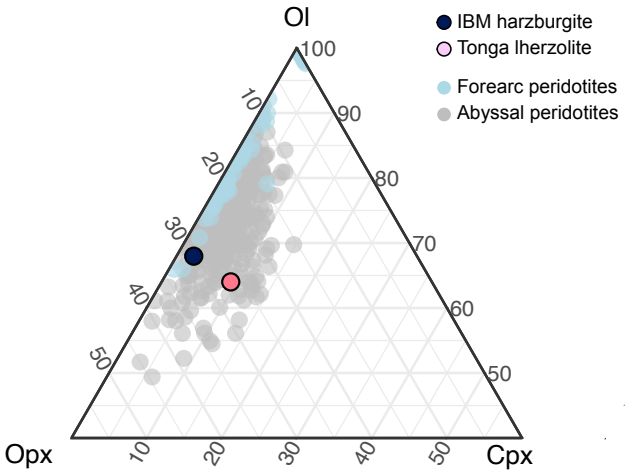

Figure S-3 Mineral modes of the IBM harzburgite (ODP125-778A-003R-CC-4–7) and Tonga lherzolite (BMRG08-111-3-6). Comparison of mineral modes among the studied samples, residual abyssal peridotites (Warren, 2016), and depleted forearc peridotites (Parkinson and Pearce, 1998; Birner *et al.*, 2017; Loocke and Snow, 2024).

Major element compositions of minerals in peridotite samples were obtained using the JEOL JXA-8900R electron microprobe at the Atmosphere and Ocean Research Institute, University of Tokyo. Analytical conditions were set at an accelerating voltage of 15 kV, 12 nA probe current, and a 3 µm beam spot for the analyses. Natural and synthetic mineral standards were used for calibration, and ZAF correction was used for data reduction. In-house mineral standards (olivine, chromian spinel, diopside, and enstatite) were measured to monitor data quality (Akizawa *et al.*, 2021). We determined Fe^{3+} content in spinel using the method that initially treats Fe as Fe^{2+} and assumes any cation excess as Fe^{3+} beyond the three cations per four oxygens. Elemental distribution mapping of the thin section was performed using an accelerating voltage of 15 kV, a probe current of 80 nA, a focused probe with a 20 µm diameter, a step size of 30 µm, and a dwell time of 100 ms. Modal mineral abundances were determined using a supervised machine learning method implemented in XMapTools (Lanari *et al.*, 2014; Lanari and Tedeschi, 2025). To obtain representative mineral modes, we performed six repeated classifications, although potential bias introduced during thin section preparation could not be eliminated (Fig. S-3).

Trace element compositions of silicates were determined by a laser ablation-inductively coupled plasma-mass spectrometry (LA-ICP-MS) (New Wave Research UP-213 laser system and Agilent 7850 ICP-MS) at Kanazawa University. A laser beam diameter of 100 µm was used for orthopyroxene, amphibole, and olivine, and either 100 µm or 55 µm was used for clinopyroxene, depending on the size, with a repetition rate of 6 or 10 Hz and an energy density of 8 J/cm². The NIST 612 standard was used as the primary calibration standard and was analysed at the beginning of each batch ($n < 8$) with a linear drift correction applied within each analytical session. Standard glass NIST 612 was used for calibration with ^{29}Si as an internal standard, based on the Si content obtained by electron microprobe analysis (Longerich *et al.*, 1996; Pearce *et al.*, 1997; Jochum *et al.*, 2011). Details of analytical procedures and quality checks were provided in Sagawa *et al.* (2022) and Tamura *et al.* (2022).

Reconstructing Primary REE Contents in Clinopyroxene

The mineral compositions of peridotites commonly reflect subsolidus re-equilibration rather than compositions at solidus conditions (Witt-Eickschen and O'Neill, 2005; Liang *et al.*, 2013; Liang *et al.*, 2021; Lin *et al.*, 2023). We corrected the REE concentrations in clinopyroxene at a given temperature using modal abundances and partition coefficients (Eq. S-1). We did not consider contributions from olivine because of their very low concentrations and partition coefficients:

$$C_{cpx}^{corrected} = \frac{\omega_{cpx}^{measured} + \omega_{opx}^{measured} \times D_{cpx/opx}^{measured}}{\omega_{cpx}^{corrected} + \omega_{opx}^{corrected} \times D_{cpx/opx}^{corrected}} \times C_{cpx}^{measured} \quad \text{(Eq. S-1)}$$

$C_{cpx}^{corrected}$ is the concentration of element i (REE) in clinopyroxene corrected for subsolidus re-equilibration at a given temperature. $\omega_{cpx}^{measured}$ and $\omega_{opx}^{measured}$ are analysed modal abundances of clinopyroxene and orthopyroxene. $D_{cpx/opx}^{measured}$ is the exchange coefficient between clinopyroxene and orthopyroxene at the sample temperature. $C_{cpx}^{measured}$ is the analysed concentration of element i in clinopyroxene. $\omega_{cpx}^{corrected}$ and $\omega_{opx}^{corrected}$ are corrected modal abundances of clinopyroxene and orthopyroxene. $D_{cpx/opx}^{corrected}$ is the exchange coefficient between clinopyroxene and orthopyroxene at a given temperature.

We estimated the exchange partition coefficient at a given temperature using the semi-empirical model (Witt-Eickschen and O'Neill, 2005) and the lattice-strain model (Sun and Liang, 2012; Yao *et al.*, 2012; Liang *et al.*, 2013; Sun and Liang, 2013). In the semi-empirical model of Witt-Eickschen and O'Neill (2005), the exchange partition coefficient for REE is described by a nonlinear regression equation:

$$\ln D_{cpx/opx} = a_0 + \frac{a_1 + a_2 \cdot N_{Na}^{cpx} + a_3 \cdot Cr_{spl}}{T_{opx\,(1.5GPa)}} \quad \text{(Eq. S-2)},$$

where: a_0 to a_3 are the regression coefficients. N_{Na}^{cpx} is the number of atoms of Na in clinopyroxene per formula unit of six oxygen. Cr_{spl} is the molar Cr/(Cr +Al) in spinel. $T_{opx\,(1.5GPa)}$ is the temperature estimated by Ca-in-orthopyroxene geothermometer at 1.5 GPa (Brey and Köhler, 1990). We used average values for each region: IBM harzburgite (N_{Na}^{cpx} = 0.0156, Cr_{spl} = 0.378) and Tonga lherzolite (N_{Na}^{cpx} = 0.0345, Cr_{spl} = 0.195). The Ca in orthopyroxene geothermometer often records lower temperatures than REE in two pyroxene for exhumed peridotite bodies that have experienced slow cooling, because Ca has a lower closure temperature than REE (Dygert and Liang, 2015). Applying the Ca in orthopyroxene geothermometer to our forearc peridotite samples would likely overestimate the extent of REE subsolidus exchange. Therefore, we used temperatures calculated from the REE-in two pyroxene geothermometer at 1.5 GPa (Liang *et al.*, 2013). The estimated temperatures were 919 ± 3 °C (1σ) for the IBM harzburgite (ODP125-778A-003R-CC-4–7) and 931°C ± 31 for the Tonga lherzolite (BMRG08-111-3-6).

For the lattice-strain model, we obtained partition coefficients using an Excel macro (Sun and Liang, 2012; Yao *et al.*, 2012; Liang *et al.*, 2013; Sun and Liang, 2013) following Lin *et al.* (2023). We used the average major compositions of clinopyroxene and orthopyroxene for each sample and used TiO_2 contents of primitive basalts (0.63 wt.% for FAB and 1.27 wt.% for EAT) with MgO > 7.5 wt.% (Ishizuka *et al.*, 2011; Todd *et al.*, 2012; Shervais *et al.*, 2019) and an H_2O content of 0.85 wt.% in FAB (Brounce *et al.*, 2021) to calculate the partition coefficient.

Using the exchange coefficients obtained by two different models, we corrected REE concentrations in clinopyroxene to temperature of 1000–1100 °C. At subsolidus temperatures, clinopyroxene can exsolve from orthopyroxene (Poldervaart and Hess, 1951; Arai, 1984). We recalculated the mineral modes at 1000–1100 °C, assuming that 5% of the orthopyroxene exsolved to clinopyroxene during the subsolidus conditions (Akizawa *et al.*, 2016). For a semi-empirical model, Pr, Tb, and Tm contents were interpolated from adjacent elements on the chondrite-normalized REE pattern. To account for uncertainty, we repeated the calculations by combining multiple parameters. We considered two sets of exchange coefficients (D) and three temperature estimates from the REE two pyroxene thermometer **(**mean, mean - 1σ, and mean + 1σ), mineral modes, and REE analyses (IBM: 7 modes, 3 analyses; Tonga 6 modes, 3 analyses). All combinations were used to correct the data over 1000–1100 °C with 10 °C increments, resulting in 3528 corrected datasets for the IBM harzburgite and 2268 for the Tonga lherzolite sample. We then calculated the mean and standard deviations to obtain the representative data to compare with the modelled clinopyroxene (Fig. S-4). Average compositions of FAB from the Ogasawara area in the IBM region (Ishizuka *et al.*, 2011; Shervais *et al.*, 2019) and EAT from the Tonga region (Todd *et al.*, 2012) were calculated using samples with MgO contents greater than 7.5 wt.%, respectively (Fig. S-4).

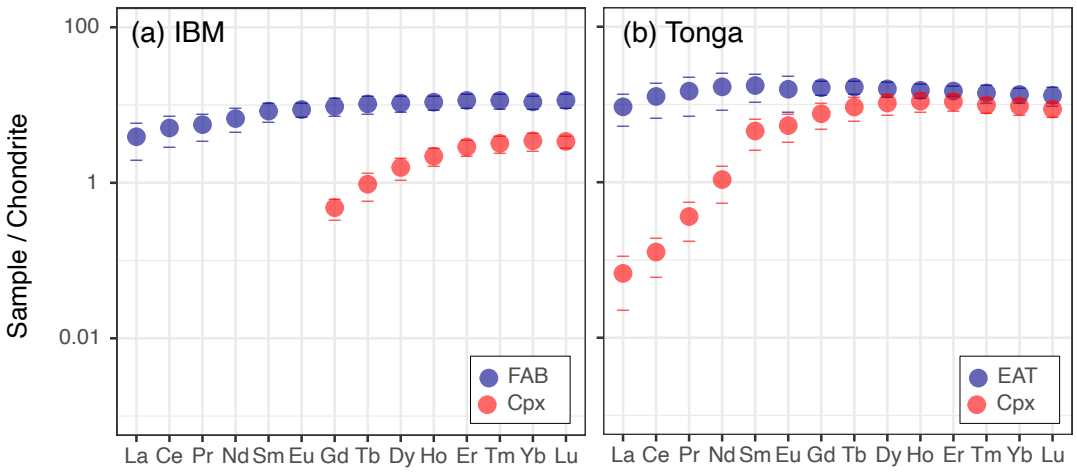

Figure S-4 Chondrite normalised REE patterns of early basalts and subsolidus-corrected clinopyroxene from the studied samples (IBM harzburgite: ODP125-778A-003R-CC-4–7, Tonga lherzolite: BMRG08-111-3-6). **(a)** the IBM region and **(b)** the Tonga region. Symbols represent average values, and error bars indicate ±2 standard deviations.

Influx-Free Open System Melting Models

We conducted a one dimensional, steady state open system melting model (Ozawa and Shimizu, 1995; Ozawa, 2001), where the full set of governing equations is described. The open system melting model encompasses batch melting, fractional melting, critical melting, melt–rock reactions, and fluid/melt flux melting, and thus it allows us to evaluate melt segregation and interaction with fluxed melt or fluids.

We conducted a suite of influx-free open system melting models to simulate REE compositions in accumulated melt and residual clinopyroxene. We used a depleted-MORB mantle (DMM) source or a depleted DMM (DDMM) source (Workman and Hart, 2005) (Table S-1). Melting mineral modes in the garnet peridotite stability field were from Walter (1998), and those in the spinel peridotite stability field were from

Kinzler and Grove (1992). Mineral modes from garnet peridotite to spinel peridotite were converted using the stoichiometry from Takazawa *et al.* (1996). We used mineral-melt partition coefficients from Kelemen *et al.* (2004), Warren (2016) and Sun and Liang (2014) (Table S-2). We first conducted influx-free open-system melting models to examine the link between our sample and early basalts (Table S-2), and we varied two key parameters (Table S-3): the critical melt fraction (a_c: 0–2%) at which melt starts to segregate, and the degree of melting (F: 0 up to 25% or until the residual clinopyroxene is exhausted). We varied the melting degree at the garnet peridotite stability field (F_{grt} = 0–10%) prior to melting at the spinel peridotite stability field. We set $\gamma = 1$ for the melt separation rate during melting and a large τ value (= 10,000) for melt separation during trapped melt crystallisation, effectively neglecting the change of melt separation rate during melting and the stage of trapped melt crystallisation. We calculated the REE contents of clinopyroxene and the accumulated total melt at every 0.1% melting increment, resulting in over 20000 modelled clinopyroxene and melt compositions (Fig. S-5 and Fig. S-6).

Table S-1 Concentrations (ppm) of REE and mineral modes of starting material (DMM and DDMM sources) and melting modes for garnet peridotite stability field and spinel peridotite stability field.

Elements	**DMM**	**DDMM**
La	0.192	0.134
Ce	0.55	0.421
Pr	0.107	0.087
Nd	0.581	0.483
Sm	0.239	0.21
Eu	0.096	0.086
Gd	0.358	0.324
Tb	0.07	0.064
Dy	0.505	0.471
Ho	0.115	0.108
Er	0.348	0.329
Yb	0.365	0.348
Lu	0.058	0.056
Mineral Mode (%)	**DMM**	**DDMM**
Olivine	59	59.3
Orthopyroxene	22	22.1
Clinopyroxene	11	10.8
Garnet	8	7.8
Melting Mode	**Garnet peridotite**	
Olivine	0.04	
Orthopyroxene	-0.19	
Clinopyroxene	1.05	
Garnet	0.1	
Melting Mode	**Spinel peridotite**	
Olivine	-0.06	
Orthopyroxene	0.28	
Clinopyroxene	0.67	
Spinel	0.11	

Table S-2 Partition coefficients used for our melting models. We set the partition coefficients for spinel zero, following Warren (2016).

Element	Kd_{ol}	Kd_{cpx}	Kd_{opx}	Kd_{grt}	Kd_{amp}
La	0.0000023	0.0550	0.0007	0.001	0.112
Ce	0.0000073	0.0876	0.0016	0.008	0.189
Pr	0.000021	0.1318	0.0032	0.033	0.294
Nd	0.000058	0.1878	0.0060	0.057	0.42
Sm	0.00029	0.3083	0.0158	0.217	0.645
Eu	0.00055	0.3638	0.0227	0.45	0.72
Gd	0.0010	0.4169	0.0315	0.9	0.769
Tb	0.0017	0.4645	0.0422	1.5	0.786
Dy	0.0029	0.5034	0.0549	2	0.77
Ho	0.0045	0.5294	0.0680	2.8	0.729
Er	0.0066	0.5437	0.0808	3.5	0.673
Yb	0.0121	0.5453	0.1036	7	0.548
Lu	0.0153	0.5373	0.1128	9	0.491

Table S-3 A summary of key input parameters for influx-free open system melting models.

Model Setup	
Figures	Fig. 4 (β = 0) Fig. S-5, S-6, S-7, S-8
Source	DMM or DDMM
Critical melt fraction (a_c)	0–2%
Melting at the garnet peridotite stability field prior to melting at the spinel peridotite stability field (F_{grt})	0–10%
Total melting degree (F)	0 to 25%, or until the residual clinopyroxene (Cpx) is exhausted.
Melting degree step	0.1%
Clinopyroxene / Accumulate melt outputs	N = 21620

Our influx-free open-system melting models show that REE concentrations in clinopyroxene decrease with increasing F (Fig. S-5). At a given F, increasing a_c suppresses LREE depletion, whereas increasing F_{grt} suppresses HREE depletion in clinopyroxene from spinel peridotite, as partition coefficients of garnet for HREE are larger than 1. LREE depletion is thus strongly controlled by a_c, and HREE depletion is controlled by F_{grt}. This observation is consistent with the previous studies (Ozawa, 2001; Hellebrand *et al.*, 2002).

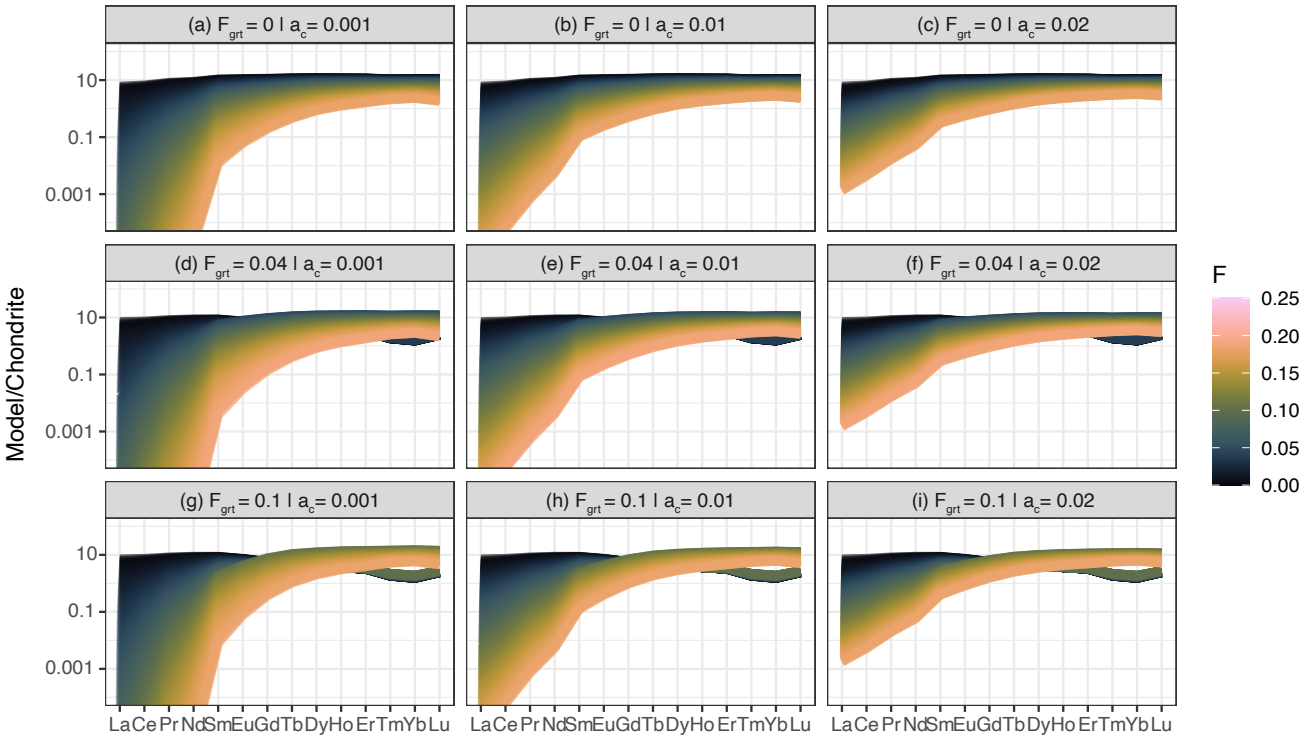

Figure S-5 Chondrite normalised REE patterns of modelled clinopyroxene from nine representative influx-free open system melting models from the DMM source. Each row corresponds to the melting degree in garnet peridotite stability field, F_{grt}, increasing from the top to bottom (0, 0.04, 0.1 = 0%, 4%, 10%). Each column represents a different critical melt fraction, a_c, increasing from left to right (0.001, 0.01, 0.02 = 0.1%, 1%, 2%). Colour indicates the degree of melting, F. Model results with low HREE contents correspond to clinopyroxene in the garnet peridotite stability field.

Accumulated melt is produced once melt separation begins, resulting in LREE enriched patterns at low a_c and low F (Fig. S-6). At a given F (< 10%), accumulated melts generated in the garnet peridotite stability field are lower in HREE than melts generated in the spinel peridotite stability field. At given F (>10%), accumulated melt shows similar REE patterns regardless of a_c and F_{grt}, while those derived from the DDMM source exhibit slightly lower REE concentrations compared to those from the DMM source. Modal Ce contents in accumulated melts are 2.98 ppm for models derived from the DDMM source and 3.86 ppm for those derived from the DMM source (Fig. S-7). The difference in source Ce between DDMM (0.421 ppm) and DMM (0.55 ppm) is 0.13 ppm, which results in a ~0.88 ppm difference in the modal Ce contents in accumulated melts. Notably, the average Ce content in FAB (3.1 ppm) is closer to the mode of the DDMM-derived accumulated melts.

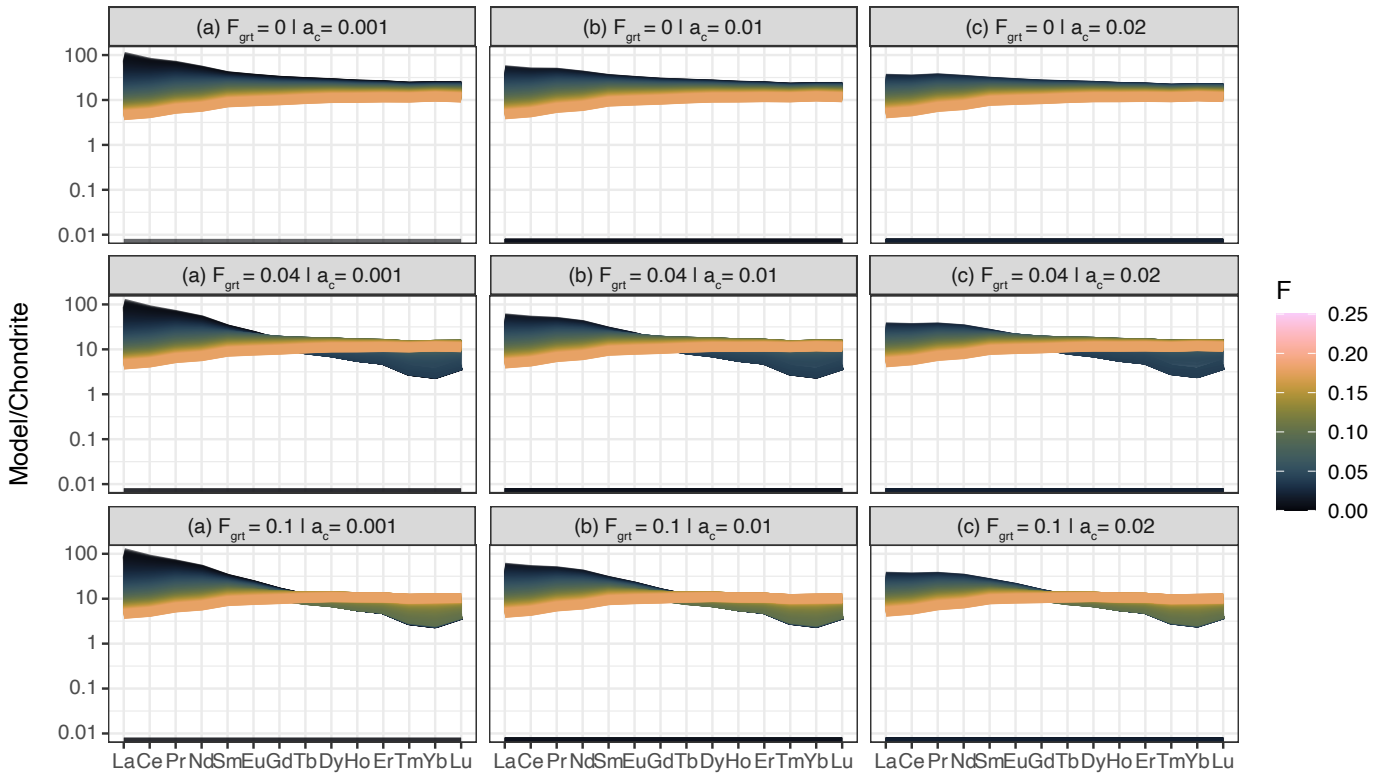

Figure S-6 Chondrite normalised REE patterns of modelled accumulated melt from nine representative influx-free open system melting models from the DMM source. The models presented here use the same parameters as in Figure S-5.

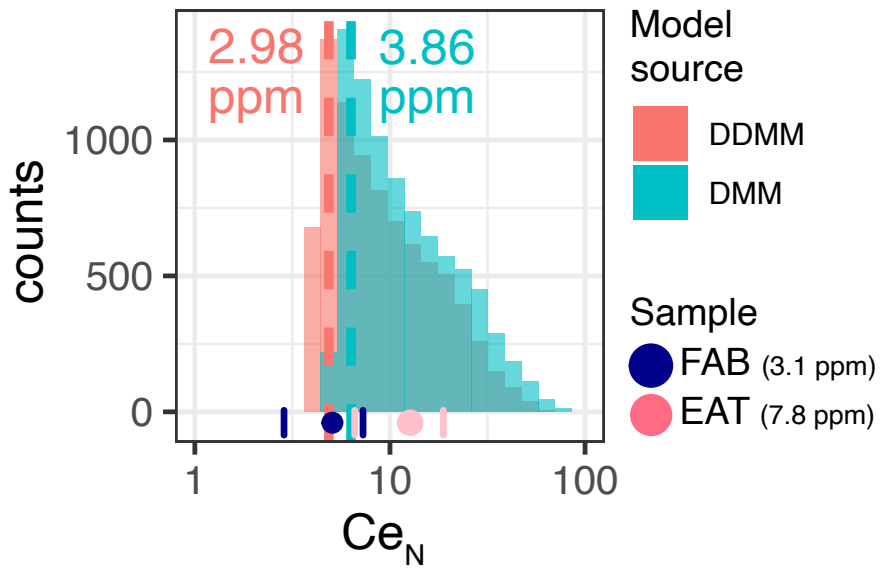

Figure S-7 Histogram of chondrite normalised Ce value (Ce_N) of modelled accumulated melt from all influx-free open system melting models, comparing models derived from the DMM and DDMM sources with FAB and EAT. Dotted lines indicate the modal Ce concentrations, estimated in log space, for models with DMM and DDMM sources. Symbols for the samples represent average values, and error bars indicate ±2 standard deviations. The corresponding average Ce concentrations (ppm) are also indicated for clarity.

Best Fit Model Estimation

To evaluate how well the modelled REE contents match the REE contents in samples, we calculate the reduced chi-square (χ_ν^2):

$$\chi_\nu^2 = \frac{1}{\nu} \cdot \sum \frac{(O_i - C_i)^2}{\sigma_i^2} \quad \text{(Eq. S-3)}$$

χ_ν^2 is the reduced chi-square, where ν is the degrees of freedom, which is the number of elements minus the number of fitted parameters, O_i represents the mean concentration of element i in the sample, σ_i is the corresponding standard deviation, and C_i is the concentration of element i in the modelled data. χ_ν^2 represents the similarity between two compositions in REE space, with a value close to 1 indicating a good fit, and we considered models with $\chi_\nu^2 < 1 + \sqrt{2/\nu}$ to represent good fits (Press *et al*., 2007).

We first compared the modelled accumulated melts with the REE compositions of FAB and EAT, respectively, and estimated best fit models that reproduce the REE patterns of FAB and EAT based on the criteria defined above. Within each region, we subsequently performed a best fit estimation by comparing modelled clinopyroxene compositions with the corrected REE compositions of clinopyroxene, using the basalt based best fit models to evaluate whether the studied samples represent residues of the corresponding basaltic melts.

We obtained the best fit models reproducing both clinopyroxene and early basalt compositions (Fig. S-8). For the IBM harzburgite and FAB, the best fits correspond to F = 16.8 ± 2.1% (2σ) with a_c = 0.4 ± 0.6% and F_{grt} = 2.9 ± 3.8%. For the Tonga lherzolite and EAT, the best fits correspond to F = 7.4% ± 0.1% with a_c = 1% and F_{grt} = 4%. Among IBM best fit models, 50.9% adopt the DDMM source and 40.9% the DMM source, whereas all Tonga best fit models are derived from the DMM source. Notably, all best fit models for the IBM clinopyroxene exhibit LREE depleted patterns, consistent with the samples in which LREE are below detection limits. The accumulated melts for the IBM FAB show slight differences in LREE contents, with models derived from the DDMM source yielding lower values than those from the DMM source.

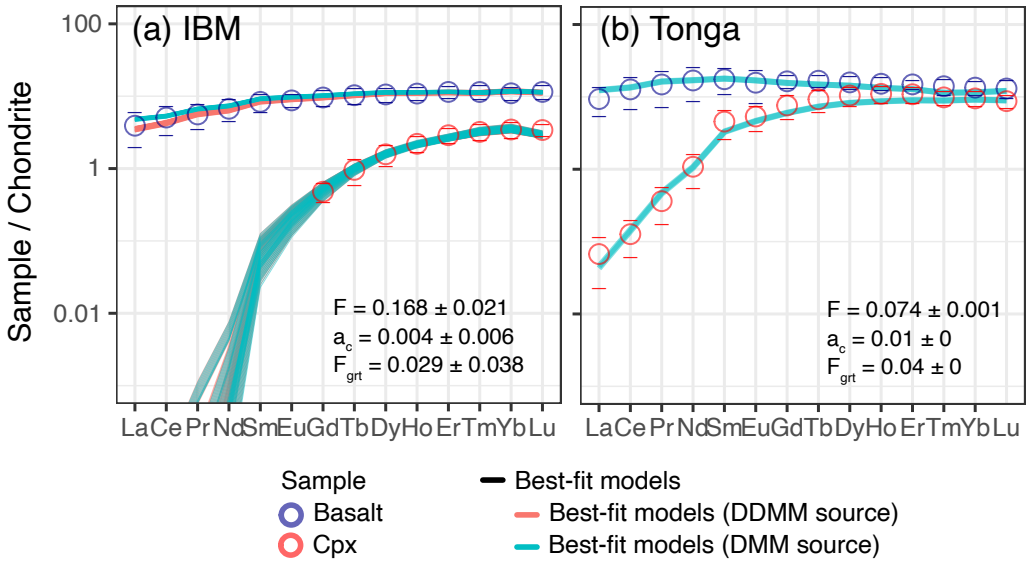

Figure S-8 Chondrite normalised REE patterns of best-fit models compared with early basalts and subsolidus corrected clinopyroxene from the studied samples (IBM harzburgite: ODP125-778A-003R-CC-4–7, Tonga lherzolite: BMRG08-111-3-6). **(a)** the IBM region and **(b)** the Tonga region. Symbols for the samples represent average values, and error bars indicate ±2 standard deviations. Mean and two standard deviations of the total melting degree (F), the critical melt fraction (a_c), and melting degree in the garnet peridotite stability field (F_{grt}) are indicated. Colour indicates the source type of each best-fit model (either DDMM or DMM).

Slab Derived Fluid Influx Open System Melting Models

Based on the best fit models estimated by influx-free open system melting models for each region, we conducted slab derived fluid influx open system melting models to investigate the effect of fluids and formation of amphibole (Table S-4). Slab derived fluid (or melt) compositions were adapted from Li *et al.* (2013) and Shervais *et al.* (2019), sourced from sediment and amphibolite (altered oceanic crust) (Table S-5). We set a_c = 0.4% and F_{grt} = 4% and varied the influx rate (β) from 0 to 1 for the IBM sample (Fig. S-9). We set a_c = 1% and F_{grt} = 4% and β = 0 to 1 for the Tonga sample (Fig. S-10). β is the mass fraction of influxed material relative to the initial solid over F. For example, when F = 10% and β =0.001 or 1, influxed mass material is 0.01% and 10%, respectively.

To examine the formation of amphibole, we considered the crystallisation of trapped melt. We assume crystallisation of olivine, clinopyroxene, and amphibole in fixed proportions of 1:4:4. Partition coefficients for amphibole are taken from Shimizu *et al.* (2017) (Table S-2). We fixed the trapped melt fraction prior to crystallisation at 0.1% and the all trapped melt is assumed to crystallise in residual solid by setting τ = 0 (*i.e.*, no melt escape during trapped melt crystallisation). The trapped melt fraction (0.1%) was therefore converted into solid phases (olivine, clinopyroxene, and amphibole) and equilibrated with the residual assemblage.

Using the parameters defined above, we modelled accumulated melt, residual clinopyroxene, and amphibole compositions up to F = 25%, at increments of 0.1% melting degree.

Table S-4 A summary of key input parameters for slab derived fluid influx open system melting models.

Model Setup	For IBM	For Tonga
Figures	Fig. 4a–b, Fig. S-9, Fig. S-11	Fig. 4c–e, Fig. S-10, Fig. S-11
Source	DDMM	DMM
Critical melt fraction (a_c)	0.4%	1%
Melting at the garnet peridotite stability field prior to melting at the spinel peridotite stability field (F_{grt})	4%	
Total melting degree (F)	0–25%	
Influx composition	Slab derived fluid (Li *et al.*, 2013; Shervais *et al.*, 2019)	
Influx rate (β)	0 (influx-free), 0.0001, 0.001, 0.01, 0.1, 1	

Table S-5 REE contents (ppm) in the slab derived fluid used for our models.

Element	
La	9.3
Ce	27.4
Pr	2.97
Nd	11.3
Sm	1.7
Eu	0.46
Gd	1.17
Tb	0.16
Dy	0.91
Ho	0.177
Er	0.499
Yb	0.515
Lu	0.08

At the best fit F (IBM: 16.8%, Tonga: 7.4%), increasing β suppresses LREE depletion in clinopyroxene, resulting in flatter REE patterns and higher absolute LREE concentrations (Fig. S-9 and Fig. S-10). Amphibole exhibits a comparable response (Fig. S-10i–l). LREE contents in clinopyroxene and amphibole are highly sensitive to small variations in β within the range of 0–0.001, but their HREE contents decrease with increasing F (Fig. S-9e–g, S-10e–g, and S-10i–k). At β is high (>0.1), even HREE depletion in clinopyroxene and amphibole is suppressed (Fig. S-9h, S-10h, and S-10l). The effect of fluid influx on the accumulated melt is comparatively minor at low β (<0.01) (Fig. S-9 and S-10). At β is high (=1), the accumulated melt exhibits LREE enriched patterns, while HREE remain broadly similar to those in models with lower β.

At higher β (~0.01) and F (>20%), the models produce LREE enriched yet HREE depleted patterns in clinopyroxene (Fig. S-9g and S-10g). These signatures resemble those observed in depleted forearc peridotites (Birner *et al.*, 2017; Loocke and Snow, 2024) and in ultra-depleted peridotites associated with boninitic magmatism, where slab derived fluid influx melting plays a key role (Nishio *et al.*, 2023).

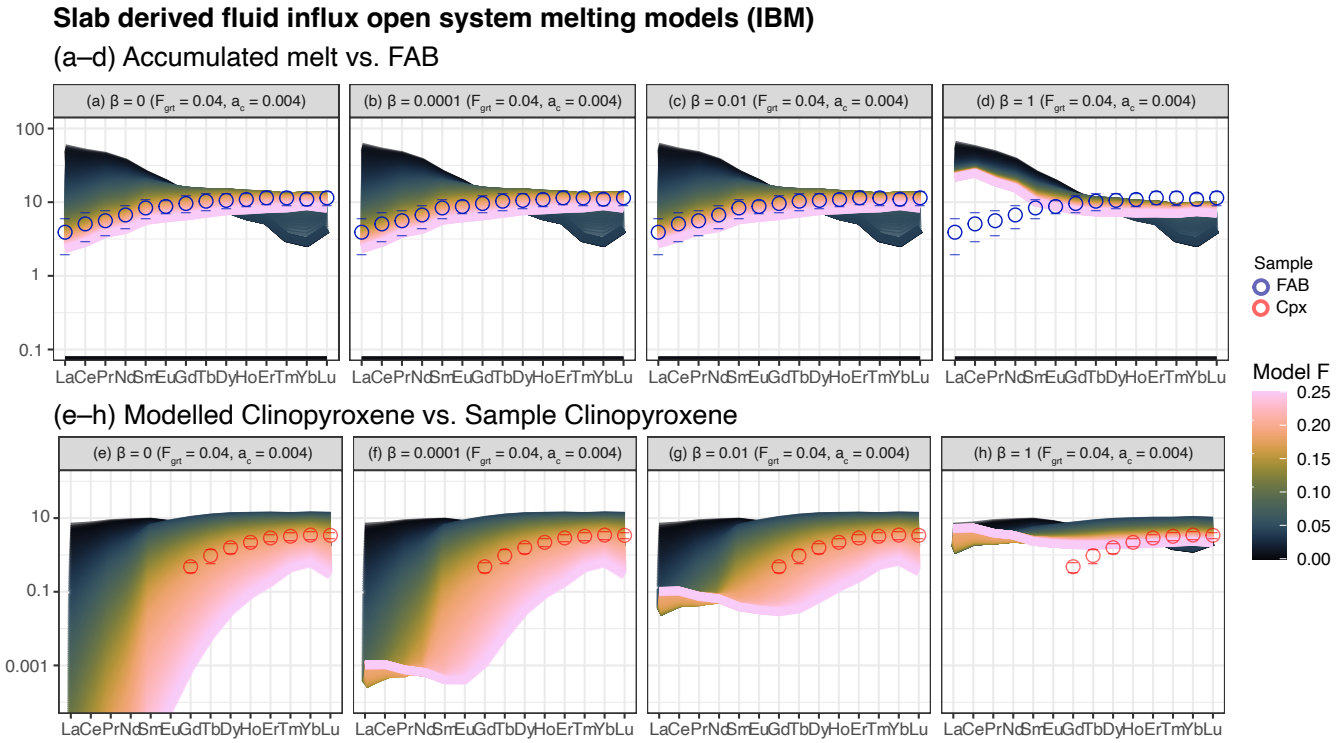

Figure S-9 Chondrite normalised REE patterns of **(a–d)** the modelled accumulated melt and **(e–h)** modelled clinopyroxene from four representative slab derived fluid influx open system melting models from the DDMM source, comparing with FAB and subsolidus corrected clinopyroxene from the studied samples (IBM harzburgite: ODP125-778A-003R-CC-4–7). Each column represents a different influx rate, β, increasing from left to right (0, 0.0001, 0.01, 1). Colour indicates the degree of melting, F. Symbols for the samples represent average values, and error bars indicate ±2 standard deviations.

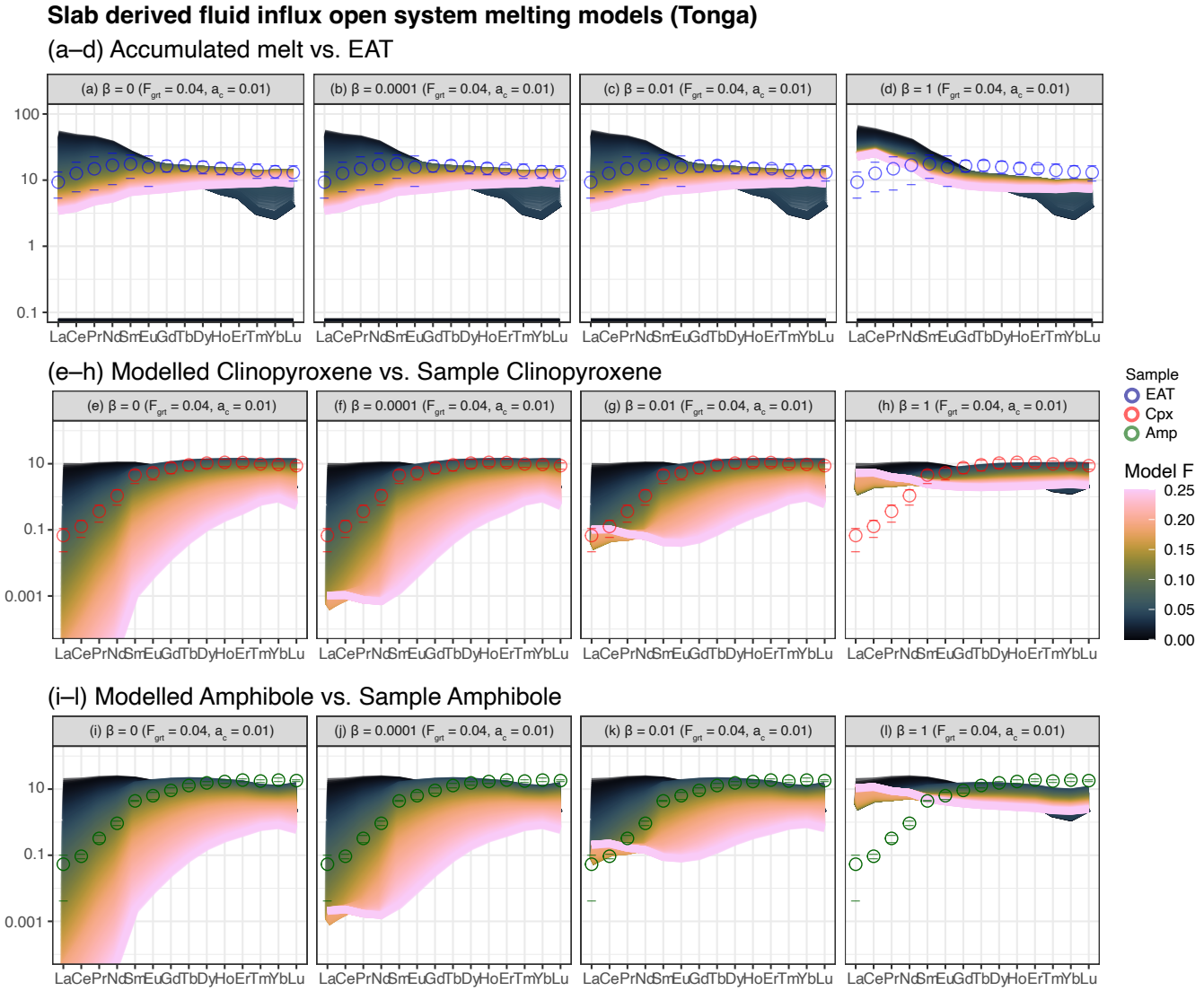

Figure S-10 Chondrite normalised REE patterns of **(a–d)** the modelled accumulated melt and **(e–h)** modelled clinopyroxene, and **(i–l)** amphibole from four representative slab derived fluid influx open system melting models from the DMM source, comparing with EAT, subsolidus corrected clinopyroxene, and amphibole from the studied samples (Tonga lherzolite: BMRG08-111-3-6). Each column represents a different influx rate, β, increasing from left to right (0, 0.0001, 0.01, 1). Colour indicates the degree of melting, F.

Figure S-11 presents REE patterns of best fit models of each region (IBM: F = 16.8%, a_c = 0.4%, F_{grt} = 4%; Tonga: F = 7.4%, a_c = 1%, F_{grt} = 4%), with varying β. At the best fit conditions, increasing β shows systematic changes in REE patterns. In both clinopyroxene and amphibole, higher β suppresses LREE depletion, whereas HREE remain relatively constant due to the low HREE concentrations in the slab derived fluid (Table S-5). Because the best fit F is higher for the IBM samples than for the Tonga samples, the suppression of LREE depletion is more pronounced at much lower β. For the IBM clinopyroxene, the detection limit of Ce corresponds to ~0.001 in chondrite normalised value, implying that β is likely <0.0001. In contrast, for the Tonga clinopyroxene, changes in REE patterns occur at relatively higher β (>0.1).

Accumulated melt compositions at the best fit conditions are only weakly affected at low β (<0.1), which indicates that clinopyroxene and amphibole are much more sensitive to small amounts of fluid influx.

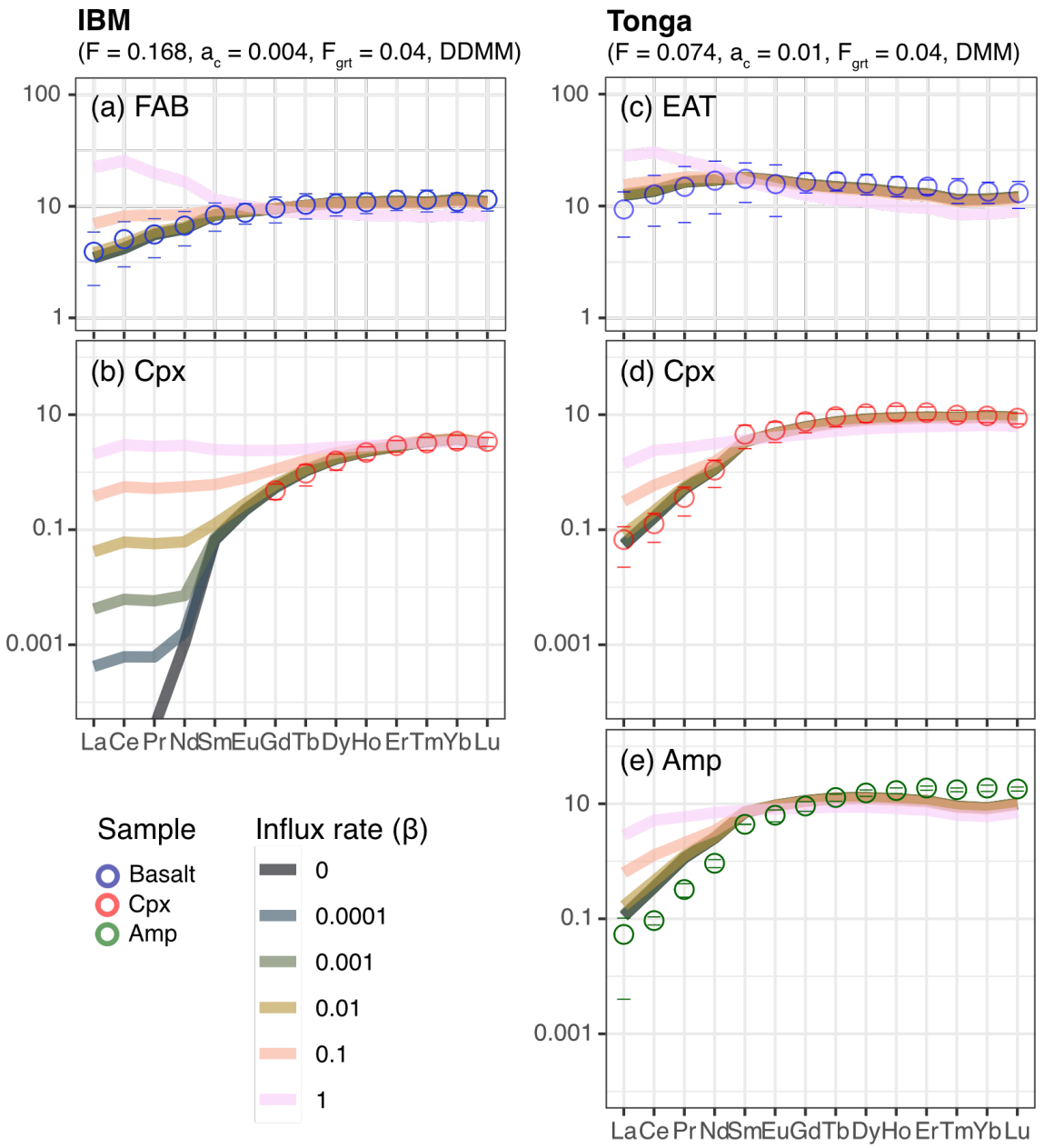

Figure S-11 Chondrite normalised REE patterns: **(a)** modelled accumulated melt compared with FAB, **(b)** modelled clinopyroxene compared with subsolidus corrected IBM clinopyroxene, **(c)** modelled accumulated melt compared with EAT, **(d)** modelled clinopyroxene compared with subsolidus corrected Tonga clinopyroxene, and **(e)** modelled amphibole compared with Tonga amphibole. Sample symbols represent average values, and error bars indicate ±2 standard deviations. All models are produced at fixed melting degree (F), critical melt fraction (a_c), and source for each region, as indicated at the top of each column. Model colour indicates the influx rate (β).

Compiled Forearc Spinel Data and Reference Data for Plots

We compiled spinel data from forearc peridotites (Table S-13), which are used in Figure 1. Data are from the IBM region (Bloomer and Hawkins, 1983; Ishii *et al.*, 1992; Parkinson and Pearce, 1998; Ishii *et al.*, 2000; D'Antonio and Kristensen, 2004; Okamura *et al.*, 2006; Zanetti *et al.*, 2006; Dare *et al.*, 2009; Murata *et al.*, 2009; Pabst, 2009; Morishita *et al.*, 2011; Harigane *et al.*, 2013; Ghosh, 2018; Debret *et al.*, 2019; Park, 2019; Albers *et al.*, 2020; Golich and Vysotskiy, 2020; Gose and Schmädicke, 2021; Ichiyama *et al.*, 2021; Miladinova *et al.*, 2023; Wang *et al.*, 2023) and the Tonga region (Birner *et al.*, 2016, 2017; Day and Brown, 2021). Spinel data from the South Mariana region were not included due to the tectonic complexity of these areas (Michibayashi *et al.*, 2009).

Reference clinopyroxene data used in Figure 2 are from the fertile residual abyssal peridotites, characterised by low spinel Cr# (0.10–0.11) and high LREE/HREE ratios in clinopyroxene, are from Johnson *et al.* (1990), Salters and Dick (2002), Seyler and Bonatti (1997), and Warren (2016). The LREE-depleted residual abyssal peridotites from Harigane *et al.* (2016). Clinopyroxene data of IBM peridotites are from Ichiyama *et al.* (2021), Ishii *et al.* (1992), Loocke and Snow (2024), and Parkinson and Pearce (1998). Clinopyroxene data of Tonga peridotites are from Birner *et al.* (2017) and Day and Brown (2021).

Reference amphibole data (Table S-14 and S-15) used for Figure 3 and S-12 are derived from IBM forearc peridotites (Ishii *et al.*, 1992; Parkinson and Pearce, 1998; Morishita *et al.*, 2011; Ichiyama *et al.*, 2021), ultra-depleted peridotites from the Kamuikotan unit, Japan (Nishio *et al.*, 2023; Tamura *et al.*, 2024), backarc peridotites (Akizawa *et al.*, 2021; Sen *et al.*, 2021; Gong *et al.*, 2022), abyssal peridotites (Seyler *et al.*, 2004; Cipriani *et al.*, 2009; Zhang *et al.*, 2024), and basal lherzolites from the Oman ophiolite (Prigent *et al.*, 2018). For comparison, we also show the compositional ranges of mid-ocean ridge basalt (MORB), backarc basin basalt (BABB), forearc basalt and early arc tholeiite (FAB-EAT), and boninite (Brounce *et al.*, 2021; Cottrell *et al.*, 2022).

The graphical abstract is adapted from Shuck *et al.* (2022) and modified to reflect the early basaltic magmatism stage.

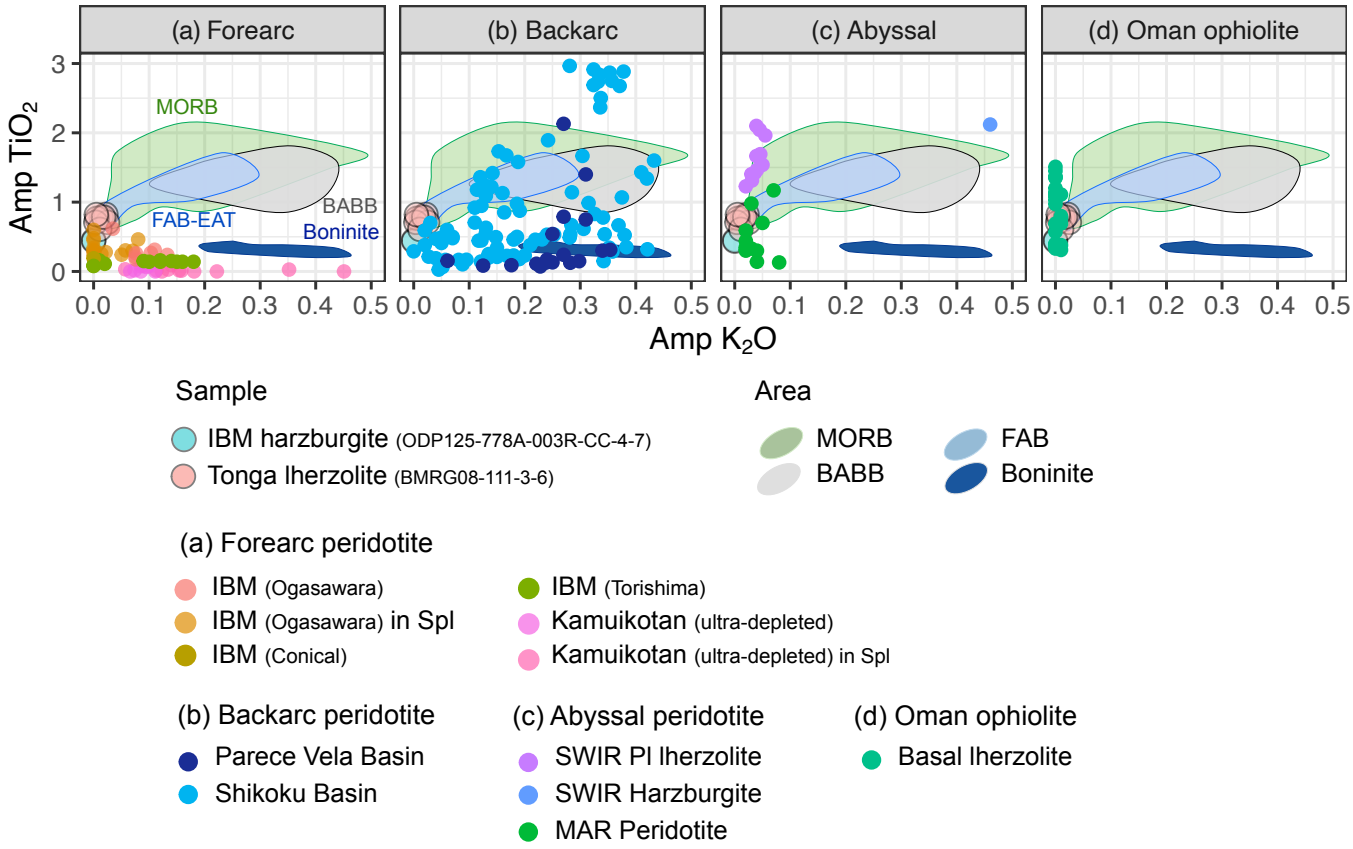

Figure S-12 TiO_2 - K_2O discrimination plot for amphibole (Ozawa, 1988) from (a) forearc and ultra-depleted peridotites, (b) backarc peridotites, (c) abyssal peridotites, and (d) basal lherzolites from the Oman ophiolite. We plotted data with SiO_2 < 52 wt.%. Compositional area for mid-ocean ridge basalt (MORB), backarc basin basalt (BABB), forearc basalt and early arc tholeiite (FAB-EAT), and boninite are presented for comparison (Brounce *et al.*, 2021; Cottrell *et al.*, 2022). For amphibole from forearc peridotites, data from the IBM (Ogasawara), IBM (Conical), and IBM (Torishima) regions are from Morishita *et al.* (2011), Parkinson and Pearce (1998), and Ishii *et al.* (1992), respectively. Data for ultra-depleted peridotites from the Kamuikotan unit are from Nishio *et al.* (2023) and Tamura *et al.* (2024). For backarc peridotites, data from the Parece Vela Basin and Shikoku Basin are from Gong *et al.* (2022), and Akizawa *et al.* (2021) and Sen *et al.* (2021), respectively. For abyssal peridotites, SWIR plagioclase lherzolite data are from Zhang *et al.* (2024), SWIR harzburgite data are from Seyler *et al.* (2004), and MAR peridotite data are from Cipriani *et al.* (2009). Data for basal lherzolites from the Oman ophiolite are from Prigent *et al.* (2018). Amphibole occurrences in IBM (Ogasawara) in Spl and Kamuikotan (ultra-depleted) in Spl peridotites represent inclusions hosted by spinel. The detection limit for K_2O in amphibole in our analyses is ~0.1 wt.%.

Supplementary Tables

Table S-6 Sample information.

Table S-7 Mineral major element chemistry.

Table S-8 Mineral trace elements contents.

Table S-9 Corrected and/or representative REE concentrations in samples.

Table S-10 Results of representative influx-free open system melting models.

Table S-11 Best fit influx-free open system melting models.

Table S-12 Result of slab derived fluid influx open system melting models.

Table S-13 Compiled spinel data from forearc peridotites.

Table S-14 Compiled amphibole major element data.

Table S-15 Compiled amphibole REE data.

Tables S-6 to S-15 (.xlsx) are available for download from the online version of this article at https://doi.org/10.7185/geochemlet.2624.

Supplementary Information References

Akizawa, N., Ozawa, K., Tamura, A., Michibayashi, K., Arai, S. (2016) Three-dimensional Evolution of Melting, Heat and Melt Transfer in Ascending Mantle beneath a Fast-spreading Ridge Segment Constrained by Trace Elements in Clinopyroxene from Concordant Dunites and Host Harzburgites of the Oman Ophiolite. *Journal of Petrology* 57, 777–814. https://doi.org/10.1093/petrology/egw020

Akizawa, N., Ohara, Y., Okino, K., Ishizuka, O., Yamashita, H., Machida, S., Sanfilippo, A., Basch, V., Snow, J.E., Sen, A., Hirauchi, K.-i., Michibayashi, K., Harigane, Y., Fujii, M., Asanuma, H., Hirata, T. (2021) Geochemical characteristics of back-arc basin lower crust and upper mantle at final spreading stage of Shikoku Basin: an example of Mado Megamullion. *Progress in Earth and Planetary Science* 8, 65. https://doi.org/10.1186/s40645-021-00454-3

Albers, E., Kahl, W.-A., Beyer, L., Bach, W. (2020) Variant across-forearc compositions of slab-fluids recorded by serpentinites: Implications on the mobilization of FMEs from an active subduction zone (Mariana forearc). *Lithos* 364–365, 105525. https://doi.org/10.1016/j.lithos.2020.105525

Arai, S. (1984) Igneous mineral equilibria in somealpine-type peridotites in Japan. In: Sunagawa, I. (Ed.) *Materials Science of the Earth's Interior.* Springer, Dordrecht, 445–460.

Birner, S.K., Warren, J.M., Cottrell, E., Davis, F.A. (2016) Hydrothermal alteration of seafloor peridotites does not influence oxygen fugacity recorded by spinel oxybarometry. *Geology* 44, 535–538. https://doi.org/10.1130/G38113.1

Birner, S.K., Warren, J.M., Cottrell, E., Davis, F.A., Kelley, K.A., Falloon, T.J. (2017) Forearc Peridotites from Tonga Record Heterogeneous Oxidation of the Mantle following Subduction Initiation. *Journal of Petrology* 58, 1755–1780. https://doi.org/10.1093/petrology/egx072

Bloomer, S.H., Hawkins, J.W. (1983) Gabbroic and Ultramafic Rocks from the Mariana Trench: An Island Arc Ophiolite. In: Hayes, D.E. (Ed.) *The Tectonic and Geologic Evolution of Southeast Asian Seas and Islands: Part 2*. American Geophysical Union, Washington, D.C., 294–317. https://doi.org/10.1029/GM027p0294

Bloomer, S.H., Wright, D., MacLeod, C.J., Tappin, D., Clift, P., Fallon, T., Fisher, R.L., Gillis, K., Ishii, T., Kelman, M., Mafi, K., Sato, H., Winowitch, M. (1996) Geology of the Tonga Forearc: A supra-subduction zone ophiolite. *EOS, Transactions, American Geophysical Union Fall Meeting*, San Francisco, California, F325 [abstract].

Brey, G.P., Köhler, T. (1990) Geothermobarometry in Four-phase Lherzolites II. New Thermobarometers, and Practical Assessment of Existing Thermobarometers. *Journal of Petrology* 31, 1353–1378. https://doi.org/10.1093/petrology/31.6.1353

Brounce, M., Reagan, M.K., Kelley, K.A., Cottrell, E., Shimizu, K., Almeev, R. (2021) Covariation of Slab Tracers, Volatiles, and Oxidation During Subduction Initiation. *Geochemistry, Geophysics, Geosystems* 22, e2021GC009823. https://doi.org/10.1029/2021GC009823

Cipriani, A., Bonatti, E., Seyler, M., Brueckner, H.K., Brunelli, D., Dallai, L., Hemming, S.R., Ligi, M., Ottolini, L., Turrin, B.D. (2009) A 19 to 17 Ma amagmatic extension event at the Mid-Atlantic Ridge: Ultramafic mylonites from the Vema Lithospheric Section. *Geochemistry, Geophysics, Geosystems* 10, Q10011. https://doi.org/10.1029/2009GC002534

Cottrell, E., Birner, S.K., Brounce, M., Davis, F.A., Waters, L.E., Kelley, K.A. (2022) Oxygen Fugacity Across Tectonic Settings. In: Moretti, R., Neuville, D.R. (Eds.) *Magma Redox Geochemistry*. American Geophysical Union, Washington, D.C., 33–61. https://doi.org/10.1002/9781119473206.ch3

D'Antonio, M., Kristensen, M.B. (2004) Serpentine and brucite of ultramafic clasts from the South Chamorro Seamount (Ocean Drilling Program Leg 195, Site 1200): inferences for the serpentinization of the Mariana forearc mantle. *Mineralogical Magazine* 68, 887–904. https://doi.org/10.1180/0026461046860229

Dare, S.A.S., Pearce, J.A., McDonald, I., Styles, M.T. (2009) Tectonic discrimination of peridotites using fO_2–Cr# and Ga–Ti–Fe^{III} systematics in chrome–spinel. *Chemical Geology* 261, 199–216. https://doi.org/10.1016/j.chemgeo.2008.08.002

Day, J.M.D., Brown, D.B. (2021) Ancient Melt-Depletion in Fresh to Strongly Serpentinized Tonga Trench Peridotites. *Journal of Petrology* 62, egab088. https://doi.org/10.1093/petrology/egab088

Debret, B., Albers, E., Walter, B., Price, R., Barnes, J.D., Beunon, H., Facq, S., Gillikin, D.P., Mattielli, N., Williams, H. (2019) Shallow forearc mantle dynamics and geochemistry: New insights from IODP Expedition 366. *Lithos* 326–327, 230–245. https://doi.org/10.1016/j.lithos.2018.10.038

Dygert, N., Liang, Y. (2015) Temperatures and cooling rates recorded in REE in coexisting pyroxenes in ophiolitic and abyssal peridotites. *Earth and Planetary Science Letters* 420, 151–161. https://doi.org/10.1016/j.epsl.2015.02.042

Ghosh, T. (2018) *Mantle Wedge Evolution Beneath the Northern Mariana Forearc*. Ph.D. Thesis, University of Houston.

Golich, A.N., Vysotskiy, S.V. (2020) Island-Arc Ophiolites of the Hahajima Seamount (Bonin Trench, Philippine Sea). *Russian Journal of Pacific Geology* 14, 221–240. https://doi.org/10.1134/S1819714020030033

Gong, X., Tian, L., Dong, Y. (2022) Contrasting melt percolation and melt-rock reactions in the Parece Vela back-arc oceanic lithosphere, Philippine Sea: A mineralogical perspective. *Lithos* 422–423, 106727. https://doi.org/10.1016/j.lithos.2022.106727

Gose, J., Schmädicke, E. (2021) Water in the Supra-Subduction-Zone Mantle of the Mariana-Izu-Bonin Forearc: Constraints From Peridotitic Orthopyroxene. *Geochemistry, Geophysics, Geosystems* 22, e2020GC009586. https://doi.org/10.1029/2020GC009586

Harigane, Y., Michibayashi, K., Morishita, T., Tani, K., Dick, H.J.B., Ishizuka, O. (2013) The earliest mantle fabrics formed during subduction zone infancy. *Earth and Planetary Science Letters* 377–378, 106–113. https://doi.org/10.1016/j.epsl.2013.06.031

Harigane, Y., Abe, N., Michibayashi, K., Kimura, J.-I., Chang, Q. (2016) Melt-rock interactions and fabric development of peridotites from North Pond in the Kane area, Mid-Atlantic Ridge: Implications of microstructural and petrological analyses of peridotite samples from IODP Hole U1382A. *Geochemistry, Geophysics, Geosystems* 17, 2298–2322. https://doi.org/10.1002/2016GC006429

Hellebrand, E., Snow, J.E., Hoppe, P., Hofmann, A.W. (2002) Garnet-field Melting and Late-stage Refertilization in 'Residual' Abyssal Peridotites from the Central Indian Ridge. *Journal of Petrology* 43, 2305–2338. https://doi.org/10.1093/petrology/43.12.2305

Ichiyama, Y., Tsujimori, T., Fryer, P., Michibayashi, K., Tamura, A., Morishita, T. (2021) Temporal and spatial mineralogical changes in clasts from Mariana serpentinite mud volcanoes: Cooling of the hot forearc-mantle at subduction initiation. *Lithos* 384–385, 105941. https://doi.org/10.1016/j.lithos.2020.105941

Ishii, T., Robinson, P.T., Maekawa, H., Fiske, R. (1992) Petrological studies of peridotites from diapiric serpentinite seamounts in the Izu-Ogasawara-Mariana Forearc, Leg 125. In: Fryer, P., Pearce, J.A., Stokking, L.B., Ali, J.R.,

Arculus, R., *et al.* (Eds.) *Proceedings of the Ocean Drilling Program, Scientific Results*, 125, Ocean Drilling Program, College Station, TX, 445–485. https://doi.org/10.2973/odp.proc.sr.125.129.1992

Ishii, T., Sato, H., Haraguchi, S., Fryer, P., Fujioka, K., Bloomer, S., Yokose, H. (2000) Petrological Characteristics of Peridotites from Serpentinite Seamounts in the Izu-Ogasawara-Mariana Forearc. *Journal of Geography (Chigaku Zasshi)* 109, 517–530. https://doi.org/10.5026/jgeography.109.4_517

Ishizuka, O., Tani, K., Reagan, M.K., Kanayama, K., Umino, S., Harigane, Y., Sakamoto, I., Miyajima, Y., Yuasa, M., Dunkley, D.J. (2011) The timescales of subduction initiation and subsequent evolution of an oceanic island arc. *Earth and Planetary Science Letters* 306, 229–240. https://doi.org/10.1016/j.epsl.2011.04.006

Jochum, K.P., Weis, U., Stoll, B., Kuzmin, D., Yang, Q., Raczek, I., Jacob, D.E., Stracke, A., Birbaum, K., Frick, D.A., Günther, D., Enzweiler, J. (2011) Determination of Reference Values for NIST SRM 610–617 Glasses Following ISO Guidelines. *Geostandards and Geoanalytical Research* 35, 397–429. https://doi.org/10.1111/j.1751-908X.2011.00120.x

Johnson, K.T.M., Dick, H.J.B., Shimizu, N. (1990) Melting in the oceanic upper mantle: An ion microprobe study of diopsides in abyssal peridotites. *Journal of Geophysical Research: Solid Earth* 95, 2661–2678. https://doi.org/10.1029/JB095iB03p02661

Kelemen, P.B., Yogodzinski, G.M., Scholl, D.W. (2004) Along-Strike Variation in the Aleutian Island Arc: Genesis of High Mg# Andesite and Implications for Continental Crust. In: Eiler, J. (Ed.) *Indisde the Subduction Factory*. American Geophysical Union, Washington, D.C., 223–276. https://doi.org/10.1029/138GM11

Kinzler, R.J., Grove, T.L. (1992) Primary magmas of mid-ocean ridge basalts 1. Experiments and methods. *Journal of Geophysical Research: Solid Earth* 97, 6885–6906. https://doi.org/10.1029/91JB02840

Lanari, P., Tedeschi, M. (2025) Chemical map classification in XMapTools. *Applied Computing and Geosciences* 25, 100230. https://doi.org/10.1016/j.acags.2025.100230

Lanari, P., Vidal, O., De Andrade, V., Dubacq, B., Lewin, E., Grosch, E.G., Schwartz, S. (2014) XMapTools: A MATLAB©-based program for electron microprobe X-ray image processing and geothermobarometry. *Computers & Geosciences* 62, 227–240. https://doi.org/10.1016/j.cageo.2013.08.010

Li, Y.-B., Kimura, J.-I., Machida, S., Ishii, T., Ishiwatari, A., Maruyama, S., Qiu, H.-N., Ishikawa, T., Kato, Y., Haraguchi, S., Takahata, N., Hirahara, Y., Miyazaki, T. (2013) High-Mg Adakite and Low-Ca Boninite from a Bonin Fore-arc Seamount: Implications for the Reaction between Slab Melts and Depleted Mantle. *Journal of Petrology* 54, 1149–1175. https://doi.org/10.1093/petrology/egt008

Liang, Y., Sun, C., Yao, L. (2013) A REE-in-two-pyroxene thermometer for mafic and ultramafic rocks. *Geochimica et Cosmochimica Acta* 102, 246–260. https://doi.org/10.1016/j.gca.2012.10.035

Liang, Y., Ji, Z., Liu, B. (2021) What can we learn from REE abundances in clinopyroxene and orthopyroxene in residual mantle peridotites? *Contributions to Mineralogy and Petrology* 176, 24. https://doi.org/10.1007/s00410-021-01780-x

Lin, K.-Y., Warren, J.M., Davis, F.A. (2023) Trace elements in abyssal peridotite olivine record melting, thermal evolution, and melt refertilization in the oceanic upper mantle. *Contributions to Mineralogy and Petrology* 178, 66. https://doi.org/10.1007/s00410-023-02044-6

Longerich, H.P., Jackson, S.E., Günther, D. (1996) Inter-laboratory note. Laser ablation inductively coupled plasma mass spectrometric transient signal data acquisition and analyte concentration calculation. *Journal of Analytical Atomic Spectrometry* 11, 899–904. https://doi.org/10.1039/JA9961100899

Loocke, M.P., Snow, J.E. (2024) Arc Foundations and Subduction Initiation: Insights into the Magmatic Evolution of the Lower Crust/Upper Mantle of the Izu–Bonin Forearc during Subduction Initiation. *Journal of Petrology* 65, egae038. https://doi.org/10.1093/petrology/egae038

Michibayashi, K., Ohara, Y., Stern, R.J., Fryer, P., Kimura, J.-I., Tasaka, M., Harigane, Y., Ishii, T. (2009) Peridotites from a ductile shear zone within back-arc lithospheric mantle, southern Mariana Trench: Results of a *Shinkai 6500* dive. *Geochemistry, Geophysics, Geosystems* 10, Q05X06. https://doi.org/10.1029/2008GC002197

Miladinova, I., Kurz, W., Hilmbauer-Hofmarcher, T. (2023) Fluid-Mantle Interaction Along the Mariana Convergent Margin. *Geochemistry, Geophysics, Geosystems* 24, e2023GC010968. https://doi.org/10.1029/2023GC010968

Morishita, T., Tani, K., Shukuno, H., Harigane, Y., Tamura, A., Kumagai, H., Hellebrand, E. (2011) Diversity of melt conduits in the Izu-Bonin-Mariana forearc mantle: Implications for the earliest stage of arc magmatism. *Geology* 39, 411–414. https://doi.org/10.1130/G31706.1

Murata, K., Maekawa, H., Yokose, H., Yamamoto, K., Fujioka, K., Ishii, T., Chiba, H., Wada, Y. (2009) Significance of serpentinization of wedge mantle peridotites beneath Mariana forearc, western Pacific. *Geosphere* 5, 90–104. https://doi.org/10.1130/GES00213.1

Nishio, I., Morishita, T., Tamura, A., Itano, K., Takamizawa, S., Ichiyama, Y., Arai, S., Barrett, N., Szilas, K. (2023) Formation of Ultra-Depleted Mantle Peridotites and Their Relationship With Boninitic Melts: An Example

From the Kamuikotan Unit, Hokkaido, Japan. *Journal of Geophysical Research: Solid Earth* 128, e2022JB025066. https://doi.org/10.1029/2022JB025066

Okamura, H., Arai, S., Kim, Y.-U. (2006) Petrology of forearc peridotite from the Hahajima Seamount, the Izu-Bonin arc, with special reference to chemical characteristics of chromian spinel. *Mineralogical Magazine* 70, 15–26. https://doi.org/10.1180/0026461067010310

Ozawa, K. (1988) Ultramafic tectonite of the Miyamori ophiolitic complex in the Kitakami Mountains, Northeast Japan: hydrous upper mantle in an island arc. *Contributions to Mineralogy and Petrology* 99, 159–175. https://doi.org/10.1007/BF00371458

Ozawa, K. (2001) Mass balance equations for open magmatic systems: Trace element behavior and its application to open system melting in the upper mantle. *Journal of Geophysical Research: Solid Earth* 106, 13407–13434. https://doi.org/10.1029/2001JB900001

Ozawa, K., Shimizu, N. (1995) Open-system melting in the upper mantle: Constraints from the Hayachine-Miyamori ophiolite, northeastern Japan. *Journal of Geophysical Research: Solid Earth* 100, 22315–22335. https://doi.org/10.1029/95JB01967

Pabst, S. (2009) *Investigation of blueschist and serpentinized harzburgite from the Mariana forearc: Insights into the mechanisms of element mobilization in subductionzones and storage of fluid-mobile elements in the mantle wedge*. Ph.D. Thesis, Heidelberg University.

Park, J.-h. (2019) *Influence of partial melting and melt-mantle interaction on PGE geochemistry of the Mariana forearc peridotites*. Ph.D. Thesis, Seoul National University.

Parkinson, I.J., Pearce, J.A. (1998) Peridotites from the Izu–Bonin–Mariana Forearc (ODP Leg 125): Evidence for Mantle Melting and Melt–Mantle Interaction in a Supra-Subduction Zone Setting. *Journal of Petrology* 39, 1577–1618. https://doi.org/10.1093/petroj/39.9.1577

Parkinson, I.J., Pearce, J.A., Thirlwall, M.F., Johnson, K.T.M., Ingram, G. (1992) Trace element geochemistry of peridotites from the Izu-Bonin-Mariana Forearc, Leg 125. In: Fryer, P., Pearce, J.A., Stokking, L.B., Ali, J.R., Arculus, R., *et al.* (Eds.) *Proceedings of the Ocean Drilling Program, Scientific Results*, 125, Ocean Drilling Program, College Station, TX, 487–506. https://doi.org/10.2973/odp.proc.sr.125.183.1992

Pearce, N.J.G., Perkins, W.T., Westgate, J.A., Gorton, M.P., Jackson, S.E., Neal, C.R., Chenery, S.P. (1997) A Compilation of New and Published Major and Trace Element Data for NIST SRM 610 and NIST SRM 612 Glass Reference Materials. *Geostandards Newsletter* 21, 115–144. https://doi.org/10.1111/j.1751-908X.1997.tb00538.x

Poldervaart, A., Hess, H.H. (1951) Pyroxenes in the Crystallization of Basaltic Magma. *The Journal of Geology* 59, 472–489. https://doi.org/10.1086/625891

Press, W.H., Teukolsky, S.A., Vetterling, W.T., Flannery, B.P. (2007) *Numerical Recipes: The Art of Scientific Computing*. Third Edition, Cambridge University Press, Cambridge.

Prigent, C., Agard, P., Guillot, S., Godard, M., Dubacq, B. (2018) Mantle Wedge (De)formation During Subduction Infancy: Evidence from the Base of the Semail Ophiolitic Mantle. *Journal of Petrology* 59, 2061–2092. https://doi.org/10.1093/petrology/egy090

Sagawa, T., Tamura, A., Okino, K., Morishita, T. (2022) Validation of Trace Element Analysis of Geological Materials by Single-Pulse Laser Ablation-Inductively Coupled Plasma-Mass Spectrometry (LA-ICP-MS). *Analytical Letters* 55, 2886–2896. https://doi.org/10.1080/00032719.2022.2077356

Salters, V.J.M., Dick, H.J.B. (2002) Mineralogy of the mid-ocean-ridge basalt source from neodymium isotopic composition of abyssal peridotites. *Nature* 418, 68–72. https://doi.org/10.1038/nature00798

Sen, A., Snow, J.E., Ohara, Y., Hirauchi, K., Kouketsu, Y., Sanfilippo, A., Basch, V., Harigane, Y., Fujii, M., Okino, K., Akizawa, N. (2021) Melting and Evolution of Amphibole-Rich Back-Arc Abyssal Peridotites at the Mado Megamullion, Shikoku Basin. *Geochemistry, Geophysics, Geosystems* 22, e2021GC010013. https://doi.org/10.1029/2021GC010013

Seyler, M., Bonatti, E. (1997) Regional-scale melt-rock interaction in lherzolitic mantle in the Romanche Fracture Zone (Atlantic Ocean). *Earth and Planetary Science Letters* 146, 273–287. https://doi.org/10.1016/S0012-821X(96)00220-8

Seyler, M., Lorand, J.-P., Toplis, M.J., Godard, G. (2004) Asthenospheric metasomatism beneath the mid-ocean ridge: Evidence from depleted abyssal peridotites. *Geology* 32, 301–304. https://doi.org/10.1130/G20191.1

Shervais, J.W., Reagan, M., Haugen, E., Almeev, R.R., Pearce, J.A., Prytulak, J., Ryan, J.G., Whattam, S.A., Godard, M., Chapman, T., Li, H., Kurz, W., Nelson, W.R., Heaton, D., Kirchenbaur, M., Shimizu, K., Sakuyama, T., Li, Y., Vetter, S.K. (2019) Magmatic Response to Subduction Initiation: Part 1. Fore-arc Basalts of the Izu-Bonin Arc From IODP Expedition 352. *Geochemistry, Geophysics, Geosystems* 20, 314–338. https://doi.org/10.1029/2018GC007731

Shimizu, K., Liang, Y., Sun, C., Jackson, C.R.M., Saal, A.E. (2017) Parameterized lattice strain models for REE partitioning between amphibole and silicate melt. *American Mineralogist* 102, 2254–2267. https://doi.org/10.2138/am-2017-6110

Shuck, B., Gulick, S.P.S., Van Avendonk, H.J.A., Gurnis, M., Sutherland, R., Stock, J., Hightower, E. (2022) Stress transition from horizontal to vertical forces during subduction initiation. *Nature Geoscience* 15, 149–155. https://doi.org/10.1038/s41561-021-00880-4

Sun, C., Liang, Y. (2012) Distribution of REE between clinopyroxene and basaltic melt along a mantle adiabat: effects of major element composition, water, and temperature. *Contributions to Mineralogy and Petrology* 163, 807–823. https://doi.org/10.1007/s00410-011-0700-x

Sun, C., Liang, Y. (2013) The importance of crystal chemistry on REE partitioning between mantle minerals (garnet, clinopyroxene, orthopyroxene, and olivine) and basaltic melts. *Chemical Geology* 358, 23–36. https://doi.org/10.1016/j.chemgeo.2013.08.045

Sun, C., Liang, Y. (2014) An assessment of subsolidus re-equilibration on REE distribution among mantle minerals olivine, orthopyroxene, clinopyroxene, and garnet in peridotites. *Chemical Geology* 372, 80–91. https://doi.org/10.1016/j.chemgeo.2014.02.014

Takazawa, E., Frey, F., Shimizu, N., Obata, M. (1996) Evolution of the Horoman Peridotite (Hokkaido, Japan): Implications from pyroxene compositions. *Chemical Geology* 134, 3–26. https://doi.org/10.1016/S0009-2541(96)00083-6

Tamura, A., Sagawa, T., Okino, K., Morishita, T. (2022) Determination of whole-rock trace-element compositions of siliceous rocks using MgO-diluted fused glass and LA–ICP–MS. *Geochemical Journal* 56, 231–239. https://doi.org/10.2343/geochemj.GJ22020

Tamura, A., Nishio, I., Iwata, Y., Arai, S., Morishita, T. (2024) Amphibole in ultra-depleted peridotites from the Horokanai ophiolite, Hokkaido, Japan: Boninite melt trapped in the mantle wedge. *Ofioliti* 49, 37–54. https://doi.org/10.4454/ofioliti.v49i1.568

Todd, E., Gill, J.B., Pearce, J.A. (2012) A variably enriched mantle wedge and contrasting melt types during arc stages following subduction initiation in Fiji and Tonga, southwest Pacific. *Earth and Planetary Science Letters* 335–336, 180–194. https://doi.org/10.1016/j.epsl.2012.05.006

Walter, M.J. (1998) Melting of Garnet Peridotite and the Origin of Komatiite and Depleted Lithosphere. *Journal of Petrology* 39, 29–60. https://doi.org/10.1093/petroj/39.1.29

Wang, Y., Deng, J., Liao, R., Chen, L., Li, D., Liu, H., Sun, W. (2023) Magnesium isotopic composition of the Mariana forearc serpentinite: Implications for Mg isotopic composition of the mantle wedge and Mg isotopic fractionation during mantle wedge serpentinization. *Chemical Geology* 624, 121428. https://doi.org/10.1016/j.chemgeo.2023.121428

Warren, J.M. (2016) Global variations in abyssal peridotite compositions. *Lithos* 248–251, 193–219. https://doi.org/10.1016/j.lithos.2015.12.023

Witt-Eickschen, G., O'Neill, H.St.C. (2005) The effect of temperature on the equilibrium distribution of trace elements between clinopyroxene, orthopyroxene, olivine and spinel in upper mantle peridotite. *Chemical Geology* 221, 65–101. https://doi.org/10.1016/j.chemgeo.2005.04.005

Workman, R.K., Hart, S.R. (2005) Major and trace element composition of the depleted MORB mantle (DMM). *Earth and Planetary Science Letters* 231, 53–72. https://doi.org/10.1016/j.epsl.2004.12.005

Wright, D.J., Bloomer, S.H., MacLeod, C.J., Taylor, B., Goodlife, A.M. (2000) Bathymetry of the Tonga Trench and Forearc: a map series. *Marine Geophysical Researches* 21, 489–512. https://doi.org/10.1023/A:1026514914220

Yao, L., Sun, C., Liang, Y. (2012) A parameterized model for REE distribution between low-Ca pyroxene and basaltic melts with applications to REE partitioning in low-Ca pyroxene along a mantle adiabat and during pyroxenite-derived melt and peridotite interaction. *Contributions to Mineralogy and Petrology* 164, 261–280. https://doi.org/10.1007/s00410-012-0737-5

Zanetti, A., D'Antonio, M., Spadea, P., Raffone, N., Vannucci, R., Bruguier, O. (2006) Petrogenesis of Mantle Peridotites from the Izu-Bonin-Mariana (IBM) Forearc. *Ofioliti* 31, 189–206. https://doi.org/10.4454/ofioliti.v31i2.340

Zhang, W.-Q., Liu, C.-Z., Dick, H.J.B., Mitchell, R.N., Liu, B.-D. (2024) Oceanic mantle beneath ultraslow spreading ridges metasomatized by variably evolved melts. *Contributions to Mineralogy and Petrology* 179, 15. https://doi.org/10.1007/s00410-023-02093-x